

Defect-induced enhanced photocatalytic activities of reduced α -Fe₂O₃ nanoblades

Honglei Feng¹, Yiqian Wang¹, Chao Wang¹, Feiyu Diao¹, Wenhui Zhu², Peng Mu², Lu Yuan², Guangwen Zhou² and Federico Rosei³

¹ College of Physics & The Cultivation Base for State Key Laboratory, Qingdao University, No. 308 Ningxia Road, Qingdao, 266071, People's Republic of China

² Department of Mechanical Engineering & Multidisciplinary Program in Materials Science and Engineering, State University of New York, Binghamton, NY 13902, USA

³ INRS-Centre for Energy, Materials and Telecommunications, 1650 Boulevard Lionel-Boulet, Varennes, Québec J3X 1S2, Canada

E-mail: yqwang@qdu.edu.cn

Received 4 January 2016, revised 3 March 2016

Accepted for publication 16 May 2016


Published 10 June 2016



CrossMark

Abstract

Bicrystalline α -Fe₂O₃ nanoblades (NBs) synthesized by thermal oxidation of iron foils were reduced in vacuum, to study the effect of reduction treatment on microstructural changes and photocatalytic properties. After the vacuum reduction, most bicrystalline α -Fe₂O₃ NBs transform into single-layered NBs, which contain more defects such as oxygen vacancies, perfect dislocations and dense pores. By comparing the photodegradation capability of non-reduced and reduced α -Fe₂O₃ NBs over model dye rhodamine B (RhB) in the presence of hydrogen peroxide, we find that vacuum-reduction induced microstructural defects can significantly enhance the photocatalytic efficiency. Even after 10 cycles, the reduced α -Fe₂O₃ NBs still show a very high photocatalytic activity. Our results demonstrate that defect engineering is a powerful tool to enhance the photocatalytic performance of nanomaterials.

 Online supplementary data available from stacks.iop.org/NANO/27/295703/mmedia

Keywords: α -Fe₂O₃ nanoblades, oxygen vacancies, dislocations, pores, photocatalytic activity

(Some figures may appear in colour only in the online journal)

Introduction

Nanostructured oxides are an emerging class of materials which exhibit a variety of useful functionalities [1–6]. In particular, hematite (α -Fe₂O₃) has been extensively studied because of its great potential for a wide range of practical applications [7–9]. For instance, it has emerged as a strong candidate material for use in photocatalysis and photo-electrochemical water splitting due to its small bandgap ($E_g = 2.2$ eV) that absorbs light with a wavelength up to 560 nm and collects up to 40% of the solar spectrum's energy, and its favorable valence band position for oxidizing water into O₂ [10, 11]. To improve photocatalytic performance, various pure α -Fe₂O₃ nanostructures have been synthesized [12, 13]. In addition, heterogeneous photocatalysts with different mass ratios of Fe₂O₃ versus TiO₂, [14] ZnO [15] and CdS [16] have also been

manufactured, exhibiting better photocatalytic activities than pure Fe₂O₃.

Recently, hematite nanostructures such as α -Fe₂O₃ nanowires and nanoblades (NBs) have been synthesized through thermal oxidation of iron (Fe) foils [17–19]. Our earlier work [19] indicated that these α -Fe₂O₃ NBs exhibit a double-layered bicrystalline structure. The atomic structure of the coincidence-site-lattice (CSL) twist boundaries in these bicrystalline α -Fe₂O₃ NBs were determined using high-resolution transmission electron microscopy (HRTEM) and their effects on the electrical properties were also studied [20]. Due to their significantly-extended surface area associated with their particular morphology, these NBs may also hold unique properties for photocatalysis which are closely related to size and morphology.

It is known that the presence of defects in semi-conductors can influence the photocatalytic activity [21].

Defects are likely generated during the reduction process of hematite [22]. Here we use vacuum annealing to reduce the double-layered α -Fe₂O₃ NBs and examine the effect of such reduction treatment on photocatalytic properties. We demonstrate that the vacuum-reduction induced microstructural defects in the α -Fe₂O₃ NBs can significantly enhance the photocatalytic efficiency. The oxygen vacancies, perfect dislocations and dense pores play important roles in the visible light photocatalysis process. This work could provide a new pathway for the design of advanced nanocatalysts with defects.

Experiment

Sample preparation

We developed a two-step process for sample preparation, consisting of (i) oxidation of sandblasted Fe foils and (ii) vacuum reduction of α -Fe₂O₃ NBs. High-purity Fe foils (99.99%) with a thickness of 0.25 mm purchased from Sigma-Aldrich were used in the oxidation experiments. The Fe foils were first sandblasted by glass bead abrasives for 9 s, and the sandblasted samples were then thoroughly rinsed with deionized water and acetone for 5 min. Subsequently the cleaned Fe foils were oxidized at 600 °C at an oxygen pressure of 250 mbar. More experimental details for the synthesis of α -Fe₂O₃ NBs can be found in our previous work [19]. The as-synthesized α -Fe₂O₃ NBs were further annealed in vacuum ($\sim 2 \times 10^{-6}$ Torr) at 700 °C for 1 h to prepare the reduced samples. The reaction of $\text{Fe}_2\text{O}_3(s) \xrightarrow[\text{vacuum}]{\Delta} \text{Fe}_2\text{O}_{3-x}(s) + \frac{x}{2}\text{O}_2(g) \uparrow$ takes place in the reduction process, which results in the loss of oxygen and concomitant formation of oxygen vacancies in the parent oxide.

TEM samples of α -Fe₂O₃ NBs were prepared by peeling off the black products from the surface of Fe foils after oxidation and reduction, then ultrasonically dispersing them in ethanol for several minutes, and dispersing a drop onto a holey-carbon-film-coated copper grid.

Characterization

The surface morphologies and crystal structures of samples were examined using an FEI Supra 55 VP field-emission scanning electron microscope (SEM) and PANalytical's X'Pert x-ray diffraction (XRD), respectively. The morphologies and microstructures of the products were examined using a JEOL JEM2100F transmission electron microscope (TEM) operated at 200 kV. The chemical composition and electronic structure were studied by electron energy-loss spectroscopy (EELS) in a Tecnai F20 TEM. All the EELS spectra were acquired in an image mode with an electron beam probe size of 1–2 nm and a half collection angle of ~ 16 mrad. The thickness (t) of the NBs is determined by $t/\lambda_P = \ln(I_t/I_0)$, where λ_P is a total mean free path for all inelastic scattering, I_0 is the area under the zero-loss peak, and I_t is the total area under the whole EELS spectrum.

The Brunauer–Emmett–Teller (BET) surface areas of both non-reduced and reduced NBs were measured by nitrogen physisorption at 77 K using an automatic volumetric sorption analyzer (NOVA 1100, Quantachrome, USA). Room-temperature UV–vis diffuse reflectance spectra (UV–vis DRS) were recorded on a HITACHI U-4100 spectrophotometer.

Photocatalytic properties

To compare the photocatalytic activities of non-reduced and reduced α -Fe₂O₃ NBs, all the photocatalysis tests were performed under the same experimental conditions. The visible light photodegradation experiments were carried out in a 50 ml test tube using rhodamine B (RhB) solution as a photocatalytic dye. Typically, 40 mg of the test sample and 1 ml H₂O₂ (30 wt%) were added into 250 ml aqueous solution of RhB (10 mg l⁻¹) to form a suspension. The initial pH of the suspension is 6.8. The suspension was magnetically stirred in the dark for 0.5 h to keep an adsorption–desorption equilibrium of the dye on the sample surface before being irradiated by a 300 W xenon lamp (100 mW cm⁻²) equipped with an ultraviolet cutoff filter ($\lambda > 420$ nm). At given irradiation time intervals inferred from the degradation rate, 4 ml of the reaction suspension was extracted. The concentration of RhB was determined by monitoring the absorbance maximum in the UV–vis absorption spectra which was recorded on a UV-3200-PC vis spectrophotometer.

The photoelectrochemical test system was composed of a CHI 660D electrochemistry potentiostat (Shanghai Chenhua Instruments, Inc., China), a 300 W xenon lamp with cutoff filters ($\lambda > 420$ nm), and a home-made three-electrode cell with a Pt foil as the counter electrode, Ag/AgCl as the reference electrode, and 1 M Na₂SO₄ as the electrolyte. The prepared samples served as the working electrodes with an exposed area of 1×1 cm².

Results and discussion

Figure 1(a) displays a representative cross-sectional SEM image of α -Fe₂O₃ NBs, indicating that dense NBs cover the surface of the oxidized Fe foil. In our previous study [19], it was found that these NBs result from the coalescence of two nanoscale islands during the oxidation process, possessing a bicrystalline structure, as apparent in figure 1(a). After the reduction in vacuum at 700 °C, dense pores are found in the reduced NBs, as shown in figure 1(b). The dimensions of the pores range from 10 nm to 300 nm. Figure S1 in the supporting information shows the XRD patterns for non-reduced and reduced α -Fe₂O₃ NBs. Both patterns match well with the rhombohedral α -Fe₂O₃ structure and show no characteristic peaks for any other phases or impurities, indicating the high purity of the products. From the phase diagram calculated for the iron-oxygen system [23], the reduced product of α -Fe₂O₃ under the conditions in the present study remains in the hematite phase, which is consistent with our XRD results.

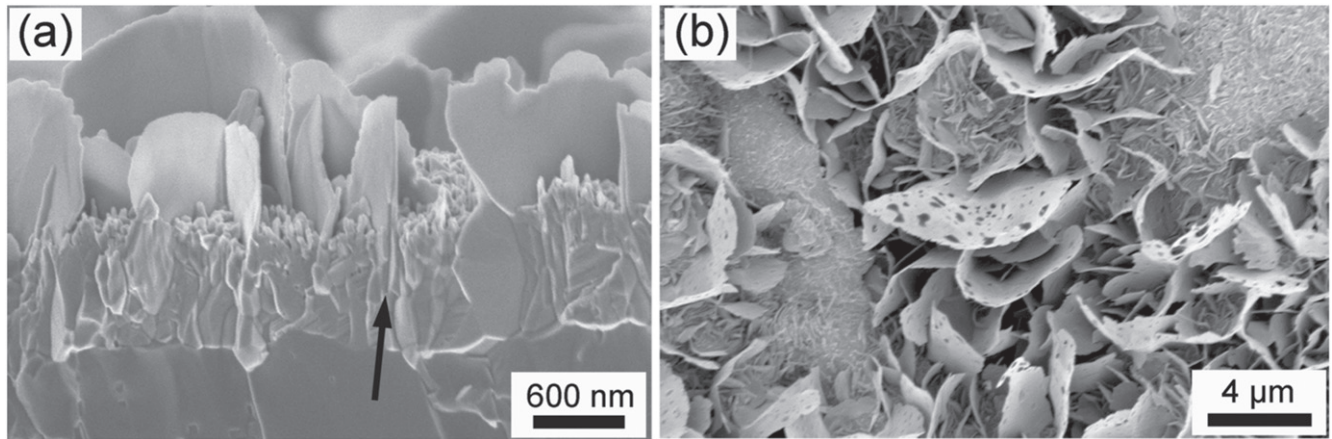


Figure 1. (a) Cross-sectional SEM image of as-produced α -Fe₂O₃ NBs after the oxidation; (b) top-view SEM image of α -Fe₂O₃ NBs after the reduction in vacuum at 700 °C.

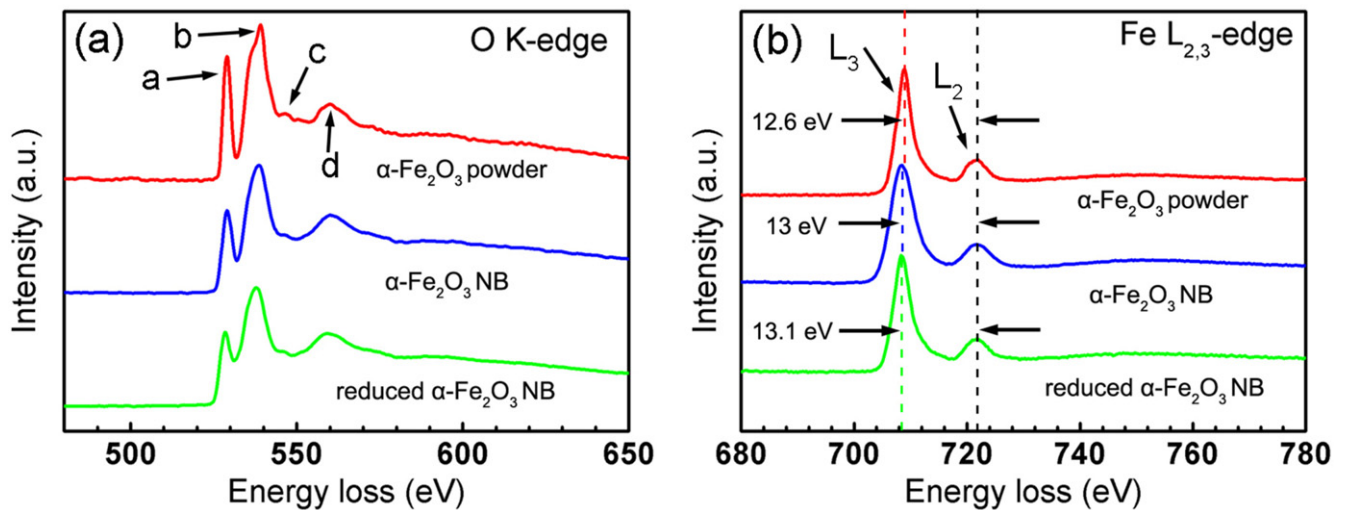


Figure 2. (a) Oxygen K-edge ELNES spectra for different Fe₂O₃ nanostructures; (b) the corresponding EELS spectra of Fe-L_{2,3} edges for different Fe₂O₃ nanostructures. All the raw data were calibrated on an energy scale and deconvoluted to reduce the multiple-scattering effect.

To study the differences in chemical compositions of α -Fe₂O₃ NBs before and after reduction, EELS was also carried out. To compare with α -Fe₂O₃ NBs before and after reduction, pure α -Fe₂O₃ powder was chosen as a counterpart to investigate the differences in the fine structures of oxygen K-edges and Fe-L_{2,3} edges. The morphology and crystal structure of α -Fe₂O₃ powders were examined by TEM (figure S2). Figure 2 shows the EELS spectra of oxygen K-edges and Fe-L_{2,3} edges for the α -Fe₂O₃ powder, bicrystalline α -Fe₂O₃ nanoblade (NB) and single-layered reduced α -Fe₂O₃ NB, respectively. For the α -Fe₂O₃ powder, all the spectra are acquired from the edge regions of the sample. However, for non-reduced and reduced NBs, all the spectra are collected from the central regions of the samples. In figure 2(a), four peaks, labeled a–d, can be found in the oxygen K-edge energy-loss near-edge fine structure (ELNES). It can be clearly seen from figure 2(a) that the intensities of both peak a and peak b evidently decrease in the following order: $I_{\text{powder}} > I_{\text{non-reduced NB}} > I_{\text{reduced NB}}$. It was previously demonstrated that the decreased intensities in peaks a and b of

EELS spectra for α -Fe₂O₃ nanostructures are associated with the oxygen vacancies inside the nanostructures [24, 25]. Thus, the lower the peak intensities in EELS spectra, the higher content of the oxygen vacancies in α -Fe₂O₃. Then it can be deduced that the reduced NBs have the highest content of oxygen vacancies while the powder has the lowest content of oxygen vacancies. In addition, the Fe-L edges can provide us with the ionization status of metal cations by determining the relative intensity and position of individual L₃ and L₂ edges, respectively [26]. The corresponding Fe L_{2,3} edge spectra for α -Fe₂O₃ powder, bicrystalline α -Fe₂O₃ NBs and single-layered reduced α -Fe₂O₃ NBs are shown in figure 2(b). Quantification of the EELS spectra in figure 2(b) shows that the intensity ratio $I(L_3)/I(L_2)$ is 5.1 ± 0.3 for the α -Fe₂O₃ powder, 4.5 ± 0.3 for the non-reduced NBs and 4.1 ± 0.3 for the reduced NBs. In addition, the separation between the L₂ and L₃ lines remains constant (~ 12.6 eV) for the α -Fe₂O₃ powder, but chemical shifts of L₃ line about 0.4 eV for the non-reduced NBs and 0.5 eV for the reduced NBs are detected. It was reported that the intensity ratio $I(L_3)/I(L_2)$

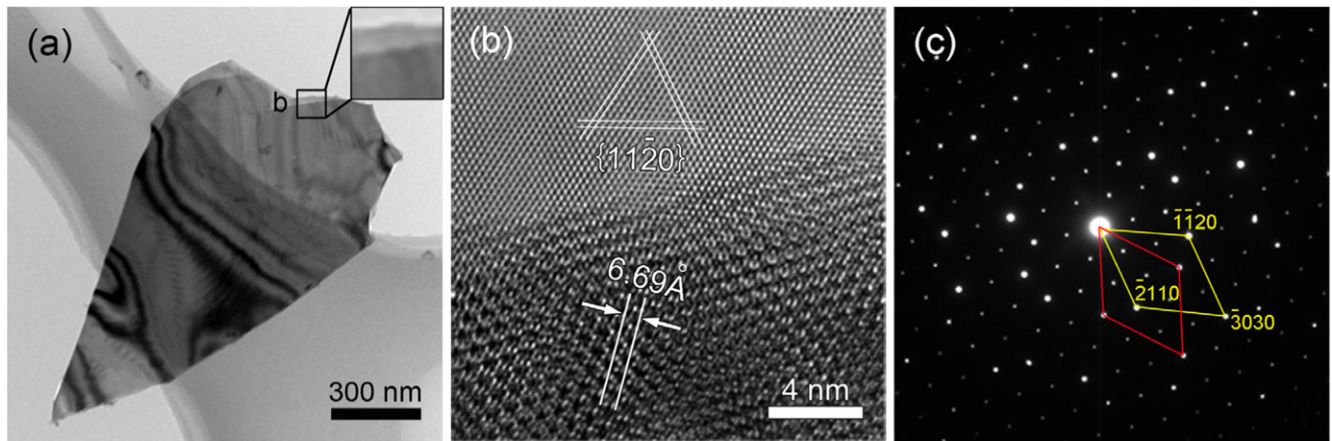


Figure 3. (a) Typical BF TEM image of an individual α -Fe₂O₃ NB. Inset shows a magnified image of the NB edge; (b) typical HRTEM image for the NB; (c) typical SAED pattern taken from the NB.

and the position of L_3 line are sensitive to the valence states of the transition metal oxide [25]. Therefore, the significant decrease in the intensity ratio $I(L_3)/I(L_2)$ and chemical shifts for the L_3 lines confirm a change in the partial oxidation states from Fe³⁺ to Fe²⁺, which is consistent with other reports [25]. Then it is concluded that more oxygen vacancies exist in the reduced NBs than in non-reduced NBs and powder. Quantification of the EELS spectra shows that the atomic ratios of Fe and O are 2:(3.00 ± 0.03) for the α -Fe₂O₃ powder, 2:(2.92 ± 0.02) for the non-reduced NBs and 2:(2.82 ± 0.03) for the reduced NBs, respectively.

To elucidate the distinct microstructures of NBs before and after the reduction, extensive TEM and HRTEM examinations were carried out on individual NBs dispersed on a holey-carbon-film-coated copper grid. Before reduction, to give a reliable occurrence frequency for bicrystalline structure, more than 100 individual NBs were examined by HRTEM, and a statistical analysis was carried out. It shows that the bicrystalline structure has a volume fraction of more than 95%. After reduction, more than 150 individual nanoblades were examined, and nearly 90% bicrystalline NBs changed into single-layered crystals.

Earlier work [20], confirmed in the present investigation, showed that CSL boundaries occur in the α -Fe₂O₃ NBs. Figure 3(a) shows a bright-field (BF) TEM image of an individual α -Fe₂O₃ NB and the inset in figure 3(a) is an enlarged image of the rectangular region. Careful examination of the α -Fe₂O₃ NB edge, as seen from the inset in figure 3(a), shows that the NB is not a single-layered but a double-layered structure. Figure 3(b) shows a typical [0001] zone-axis HRTEM image from the α -Fe₂O₃ NB edge as marked by the black rectangle region 'b' in figure 3(a). This HRTEM image clearly shows two parts, the upper part being a single-layered lattice image of α -Fe₂O₃ and the lower part being Moiré fringes contrast formed by the overlap of double-layered crystal lattices. From the HRTEM image in figure 3(b), the distance between the Moiré fringes is measured to be 6.69 Å. Figure 3(c) displays a selected-area electron diffraction (SAED) pattern taken from the NB in figure 3(a), containing two sets of [0001] zone-axis diffraction spots that can be

indexed using the lattice parameters of α -Fe₂O₃ ($a = b = 5.028$ Å, $c = 13.730$ Å, $\alpha = \beta = 90^\circ$, $\gamma = 120^\circ$). These two sets of diffraction spots rotate against each other with a rotation angle of 21.79°. Thus, this NB has a bicrystal structure, and the twist angle between the two layered crystals is 21.79°. To distinguish the two sets of diffraction spots, they are marked by red lines and yellow lines, respectively. To prove that the Moiré fringes result from the overlap of two identical (0001) α -Fe₂O₃ crystals with a twist angle, the following equation [27]

$$d_m = \frac{d_1 d_2}{\sqrt{d_1^2 + d_2^2 - 2d_1 d_2 \cos \theta}} \quad (1)$$

is adopted to calculate the space (d_m) between the Moiré fringes. In this equation, d_1 and d_2 are the lattice spacings of $\{11\bar{2}0\}$ planes of α -Fe₂O₃ ($d_1 = d_2 = 2.514$ Å), and θ is the twist angle ($\theta = 21.79^\circ$). The calculated spacing d_m between the Moiré fringes is 6.65 Å, which is in good agreement with the measured values from both HRTEM image in figure 3(b) and SAED pattern in figure 3(c). Therefore, the Moiré fringes in figure 3(b) are produced by the twist of two identical (0001) α -Fe₂O₃ crystals.

After the reduction in vacuum, most CSL boundaries in the NBs disappear and most double-layered NBs transform into single-layered NBs. The reduction reaction starts from the CSL boundaries in the bicrystalline α -Fe₂O₃ NBs due to their high-energy properties. As the binding force between the {0001} planes becomes weak during the reduction process, shear slipping might occur between the {0001} planes. Subsequently the bicrystalline NBs might separate into single-layered NBs after the reduction process. Figure 4(a) shows a typical BF TEM image of a single-layered reduced NB oriented along the [0001] direction, as seen from the SAED pattern in the inset of figure 4(a). To clarify the microstructure of the reduced NBs, extensive HRTEM examinations were carried out on individual NBs. Figure 4(b) shows a typical [0001] zone-axis HRTEM image of the reduced NB edge as marked by a black rectangle in figure 4(a). This HRTEM image clearly shows five edge-dislocation dipole pairs, which are indicated by D1 to D10. Every two dislocations constitute

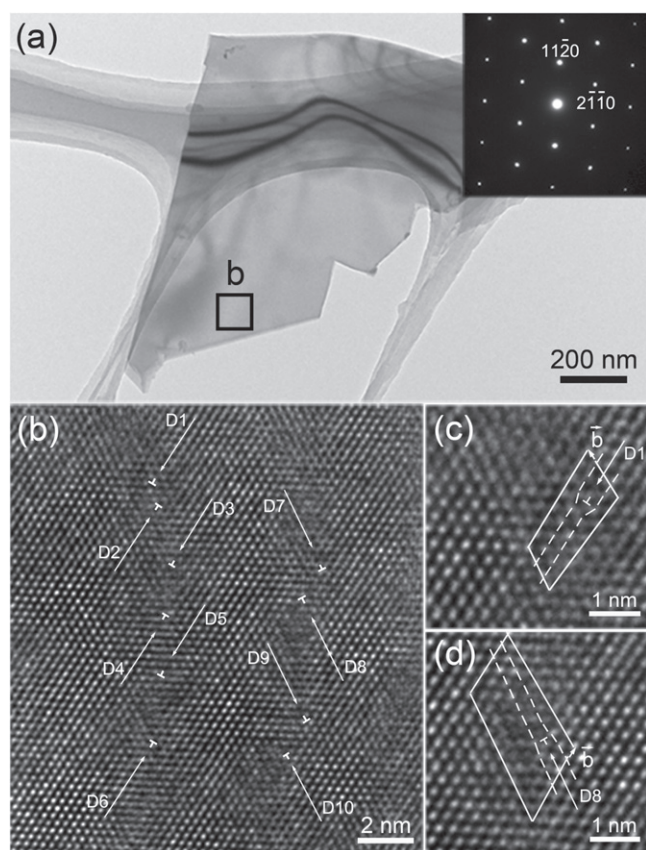


Figure 4. (a) Typical BF TEM image of a single-layered reduced α - Fe_2O_3 NB. Inset is an SAED pattern from the rectangular region; (b) typical HRTEM image of dislocation dipoles of reduced α - Fe_2O_3 NBs in rectangular region 'b'; (c) Burgers circuit for edge dislocation D1; (d) Burgers circuit for edge dislocation D8.

a dipole pair. To identify the extra half atomic planes more clearly, two enlarged HRTEM images of edge dislocations D1 and D8 are shown in figures 4(c) and (d), respectively. There are gaps between the starting and ending points of the Burgers circuits, which are indicated by arrows. The Burgers vectors for D1 and D8 are determined to be $\mathbf{b} = \frac{a}{3}\langle 10\bar{1}0 \rangle$, which is a characteristic vector for a perfect dislocation in a rhombohedral structure. As we all know, Fe cations in the α - Fe_2O_3 lattice are located at octahedral sites whose size is comparable to that of the Fe cation [28]. The vacuum-reduction treatment leads to the removal of oxygen anions from the lattice and results in an increase of Fe/O ratio. In this way, some Fe cations can be displaced to the tetrahedral sites whose size is much smaller than that of the octahedral sites. To relieve the strain arising from the lattice distortion, dislocations will form. In addition, the perfect dislocations (dipoles) usually terminate at the surfaces of the reduced NBs since the single-layered NBs are very thin (~ 10 nm).

The porous feature of single-layered reduced α - Fe_2O_3 NBs is further confirmed by the BF TEM image in figure 5(a). The reduced NBs with randomly-distributed pores look like a sieve. The pores are 10–150 nm in size which is consistent with the SEM results. Along the [0001] direction, the projected shape of most pores in the reduced NBs is close to a

trapezoid, and the enlarged TEM image of one pore is shown in the upper-right inset of figure 5(a). The lower-left inset is the [0001] zone-axis SAED pattern taken from the reduced NB, which can be indexed using the lattice parameters of α - Fe_2O_3 . After careful examinations of the SAED pattern and the facets of the pores, it can be determined that the side facets of the pores are dominated by $\{11\bar{2}0\}$ and $\{1\bar{1}00\}$ surfaces. From a typical HRTEM image of the reduced α - Fe_2O_3 NB in figure 5(b), the pore structure can be seen evidently. In the region close to the pore edges, $\{11\bar{2}0\}$ and $\{1\bar{1}00\}$ planes are parallel to the upper and right edge facets, further confirming that the side facets of the pores are dominated by $\{11\bar{2}0\}$ and $\{1\bar{1}00\}$ planes. The three-dimensional shape of the pore structure is schematically presented in the inset of figure 5(b). Analyses of the above EELS and TEM results reveal that the reduced NBs are highly defective. Under the high temperature vacuum annealing, some defects such as oxygen vacancies move to energetically more favorable positions. Then high concentration of vacancies under annealing conditions agglomerate to form pores with low-index surfaces such as $\{11\bar{2}0\}$ and $\{1\bar{1}00\}$ to reduce the surface energy. So we postulate that the pores evolve within the reduced NBs via the agglomeration of the oxygen vacancies within the defective NBs.

To understand the relationship between the microstructure and photocatalytic properties of α - Fe_2O_3 nanostructures, the photocatalytic activities of the non-reduced and reduced α - Fe_2O_3 NBs were investigated through the degradation of RhB in the presence of hydrogen peroxide (H_2O_2). The addition of H_2O_2 (Fenton reagent) is beneficial to produce hydroxyl radicals which can enhance the degradation of organic pollutants. In addition, α - Fe_2O_3 powder was chosen for comparison. Figure 6 shows the UV–vis absorption spectra of an aqueous solution of RhB photodegraded by α - Fe_2O_3 powder, non-reduced α - Fe_2O_3 NBs and reduced α - Fe_2O_3 NBs, respectively. Figure 6 shows that after 150 min irradiation under visible light, $\sim 100\%$ RhB was photodegraded by the reduced NBs. However, after 180 min irradiation under visible light, only $\sim 40\%$ RhB was photodegraded by α - Fe_2O_3 powder and $\sim 80\%$ RhB was photodegraded by non-reduced NBs. Therefore, in comparison with the α - Fe_2O_3 powder, the non-reduced and reduced NBs exhibit much better photodegradation ability over the model dye RhB, especially for the reduced NBs. To further compare the reactivity of non-reduced and reduced NBs quantitatively, their reaction rate constants (k) were calculated based on pseudo-first-order reaction kinetics, which is shown in figure 6(d). To explore the intrinsic photoreactivity, k is normalized to the specific surface area, referred to as k_s [29]. The physicochemical properties of non-reduced and reduced α - Fe_2O_3 NBs are summarized in table 1. As shown in table 1, the reaction rate constant k for the reduced α - Fe_2O_3 NBs is approximately three times that of non-reduced NBs. The reduced NBs exhibit the greatest photoreactivity with $k_s = 4.172 \times 10^{-3} \text{ min}^{-1} \text{ Lm}^{-2}$, while k_s is $2.047 \times 10^{-3} \text{ min}^{-1} \text{ Lm}^{-2}$ for the non-reduced NBs.

To evaluate the photocatalytic efficiency more precisely, photonic efficiency (quantum efficiency) is adopted. The

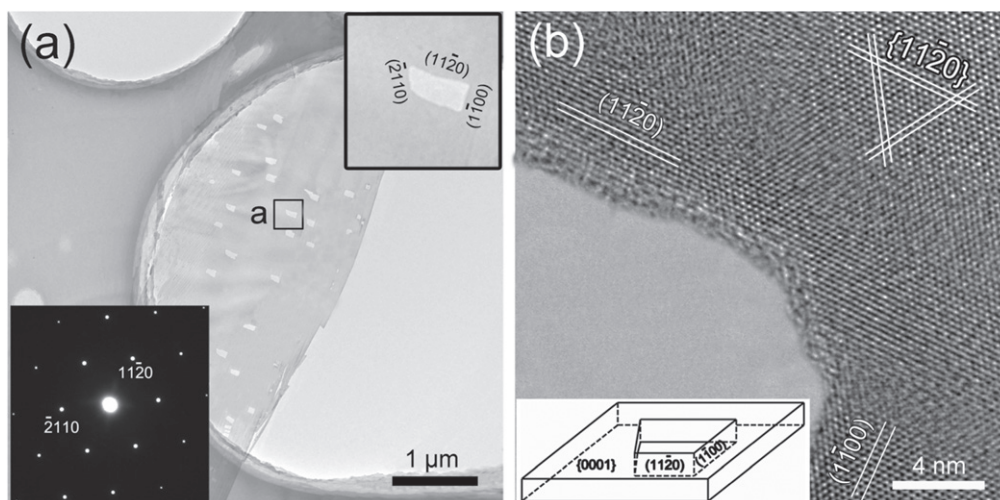


Figure 5. (a) Typical BF TEM image of a single-layered reduced α -Fe₂O₃ NB with pores. The upper-right corner inset is a magnified image of the region 'a', and the lower-left corner inset is the corresponding SAED pattern; (b) typical HRTEM image of the enlarged rectangle region 'a' in (a). The inset is a drawing of the pore structure.

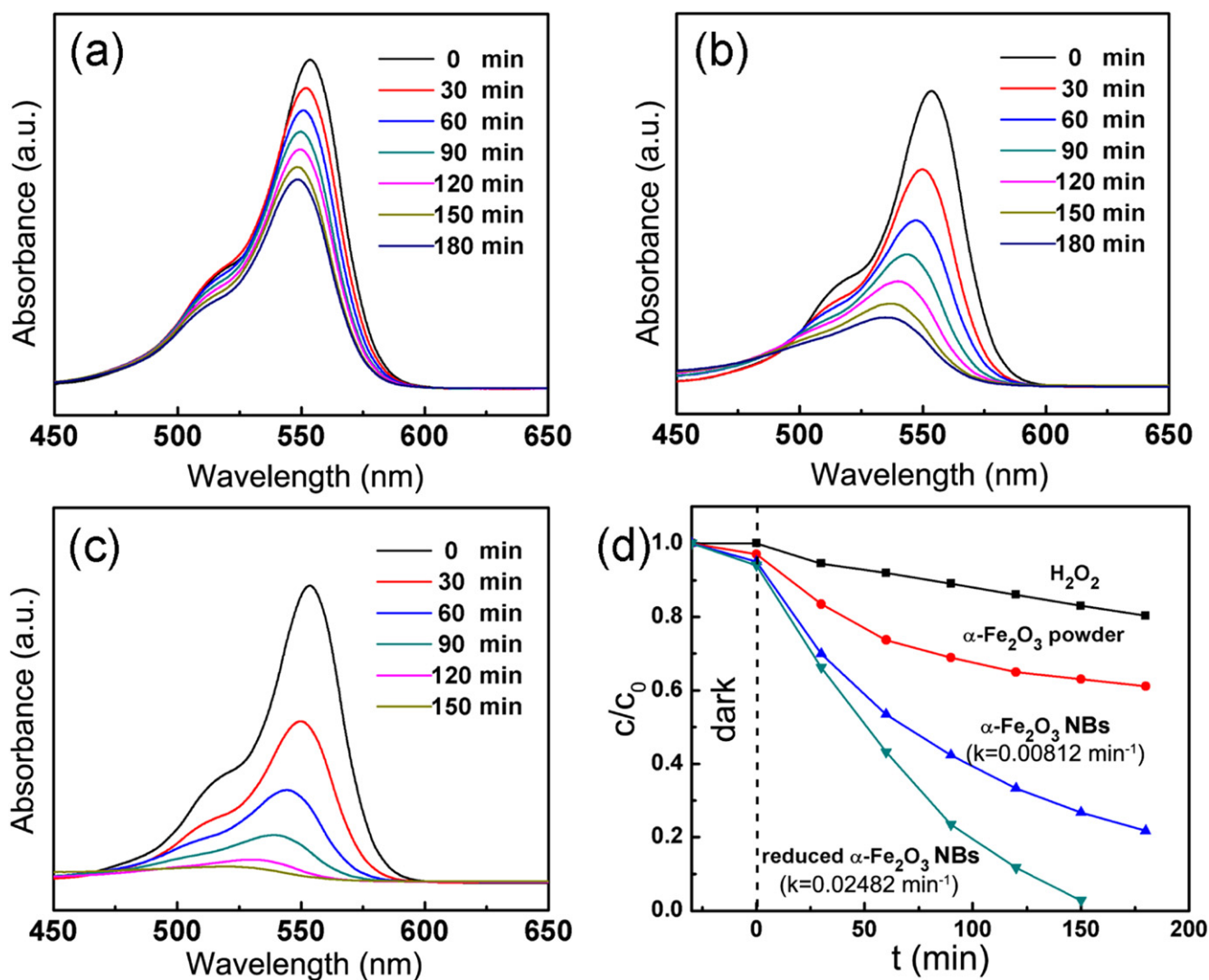


Figure 6. UV-vis absorption spectra of an aqueous solution of RhB with α -Fe₂O₃ powder (a), non-reduced bicrystalline α -Fe₂O₃ NBs (b) and reduced α -Fe₂O₃ NBs (c) in the presence of H₂O₂ additive; (d) comparison of the photocatalytic activities of α -Fe₂O₃ powder, non-reduced NBs and reduced of NBs in the presence of H₂O₂ additive.

Table 1. Physicochemical properties of non-reduced and reduced α -Fe₂O₃ NBs.

Sample	SSA ^a [m ² g ⁻¹]	Reaction rate constant k [$\times 10^{-3}$ min ⁻¹]	Normalized rate constants k_s^b [$\times 10^{-3}$ min ⁻¹ Lm ⁻²]
Non-reduced NBs	24.791	8.120	2.047
Reduced NBs	37.184	24.82	4.172

^a BET specific surface area (SSA) is calculated from figure S3 in the supporting information.

^b k_s denotes the rate constant (k) normalized to SSA, $k_s = k(\text{catalyst concentration} \times \text{SSA})^{-1}$.

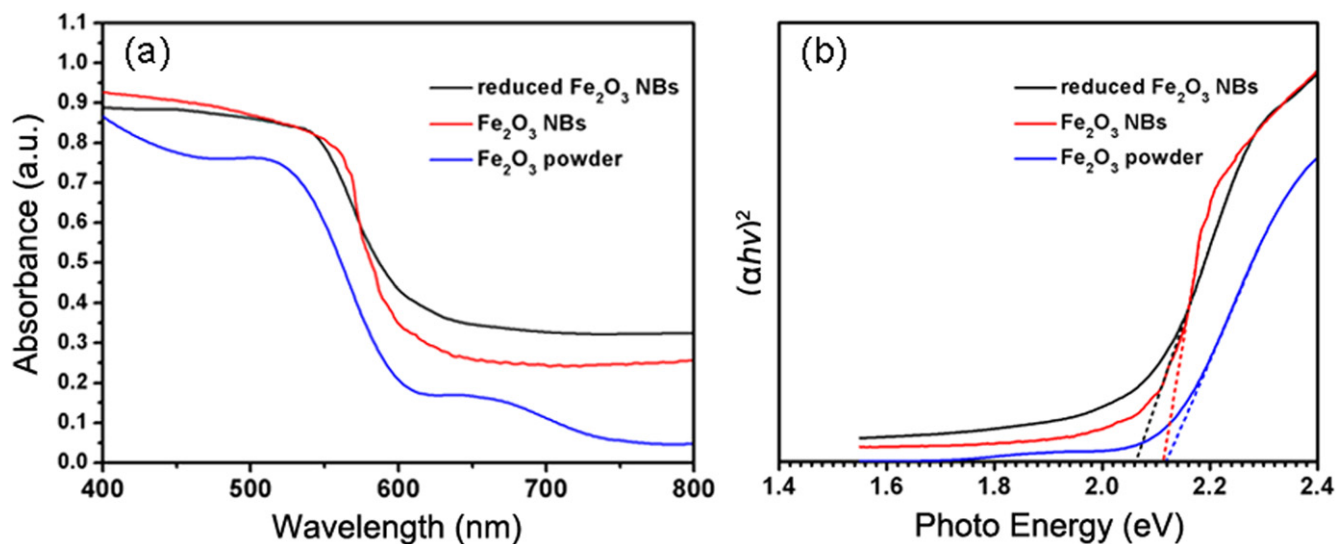


Figure 7. (a) UV-vis spectra for different Fe₂O₃ nanostructures; (b) bandgap evaluation from the plot of $(\alpha h\nu)^2$ versus the energy of the absorbed light for different Fe₂O₃ nanostructures.

photonic efficiency ξ , which is defined as the ratio of the dye degradation rate and the incident photon flux at a given wavelength, is calculated according to equations (2)–(4) based on previous literature [30, 31].

$$\xi = \frac{\text{degradation rate} [\text{mol s}^{-1}]}{\text{photon flux} [\text{mol} h\nu \text{ s}^{-1}]} = \frac{\Delta C \cdot V}{\Delta t \cdot I_0 \cdot A} \quad (2)$$

$$I_0 = \frac{I \cdot \lambda}{N_A \cdot h \cdot c} \quad (3)$$

$$\text{So, } \xi = \frac{\Delta C \cdot V N_A \cdot h \cdot c}{\Delta t \cdot I \cdot \lambda \cdot A} \quad (4)$$

where $\Delta C/\Delta t$ is the degradation rate, V the volume of the employed test solution, I_0 the photon flux, A the illuminated area, I the light intensity (100 mWcm⁻²), λ the incident wavelength (420 nm), N_A Avogadro's constant, h Planck's constant and c the velocity of light. The calculated photonic efficiencies ξ are 0.0156% and 0.0099% for the reduced and non-reduced NBs, respectively. The values of ξ for non-reduced and reduced NBs are underestimated because the incident photons can be scattered by the suspended NBs in an aqueous solution.

To verify the stability of the reduced α -Fe₂O₃ NBs, cycling photodegradation tests were carried out, and the cycling test results were shown in figure S4 in the supporting information. As shown in figure S4, even after ten cycles, the degradation rate was almost constant, confirming that reduced

α -Fe₂O₃ NBs are inherently stable during prolonged photocatalytic reactions.

To account for the enhanced photocatalytic activities of the reduced NBs, we elaborate on the effects of three different defects on the photocatalytic efficiency.

First, we focus on the effect of oxygen vacancies on the photocatalytic activities. To explore the effect and photo-reaction mechanism of oxygen vacancies, the optical properties of different Fe₂O₃ nanostructures were investigated. Figure 7(a) shows UV-vis spectra of reduced NBs, non-reduced NBs and α -Fe₂O₃ powder. Although three nanostructures show similar optical properties, reduced NBs exhibit stronger absorption in the range of 600–800 nm, which was attributed to the oxygen vacancies [32, 33]. Figure 7(b) is the plot of $(\alpha h\nu)^2$ versus the energy of the absorbed light for α -Fe₂O₃ powder, non-reduced NBs and reduced NBs. From figure 7(b), the bandgap is determined to be 2.06 eV for the reduced NBs, slightly smaller than that of the non-reduced NBs (2.11 eV) and powder (2.12 eV).

According to the results from UV-vis measurements, the effect of oxygen vacancies can be explained as follows. The oxygen vacancies do not change the bandgaps of Fe₂O₃ nanostructures significantly, but they can trap the photo-generated electrons and adsorb O₂ molecules which could be reduced into $\cdot\text{O}_2^-$ [32]. The oxygen-vacancy-involved photocatalytic reactions can be described by equations (5)–(7)



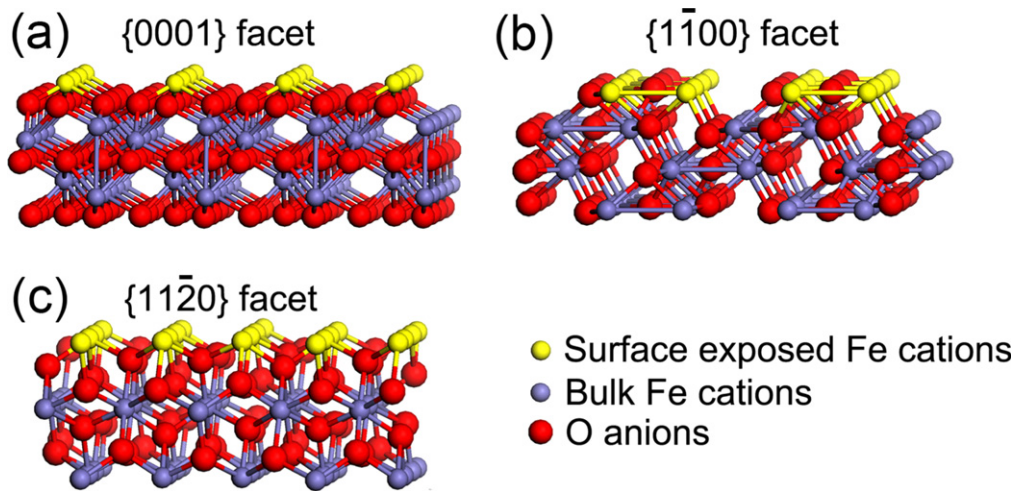
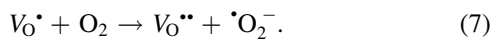


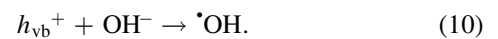
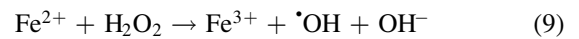
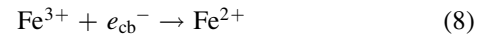
Figure 8. Surface atomic structures of {0001} (a), {1 $\bar{1}$ 00} (b) and {11 $\bar{2}$ 0} (c) facets for α -Fe₂O₃.



When the NBs are irradiated by visible light with an energy higher than or equal to the bandgap, an electron (e^-) in the valence band (VB) can be excited to the conduction band (CB) with simultaneous generation of a hole (h^+) in the VB, as shown in equation (5). The oxygen vacancy ($V_O^{\bullet\bullet}$) defects act as electron acceptors and can trap photogenerated electrons temporarily (equation (6)). Subsequently, the photoelectron can be easily trapped by electron acceptors such as adsorbed O_2 , to further produce a superoxide radical anion ($\cdot O_2^-$), as shown in equation (7). According to these equations, more oxygen vacancies can generate more $\cdot O_2^-$ which could effectively oxidize the dye of RhB [34]. Our EELS results show that more oxygen vacancies exist in the reduced NBs. Therefore, it is reasonable for the reduced NBs to show better photocatalytic performance.

Second, the porous structures observed in the single-layered reduced NBs can increase the specific surface areas. From the BET analysis, the specific surface area for the reduced NBs ($37.184 \text{ m}^2 \text{ g}^{-1}$) is more than that for the non-reduced NBs ($24.791 \text{ m}^2 \text{ g}^{-1}$). The larger specific surface areas of the reduced NBs can result in more unsaturated surface coordination sites exposed to the solution and degrade more dye molecules under the visible-light irradiation. Therefore, the reduced NBs with higher specific surface areas show enhanced photocatalytic activity. In addition, the exposed Fe cations on the surfaces also play an important role in the photocatalytic process [35]. According to our TEM results, the non-reduced NBs mainly display {0001} facets, while for the reduced NBs, apart from {0001} facets, {1 $\bar{1}$ 00} and {11 $\bar{2}$ 0} facets are also exposed. For {0001} facets with an Fe termination layer, the density of low-coordinate surface Fe cations is 4.6 atoms/nm², as shown in figure 8(a). The densities of Fe cations on {1 $\bar{1}$ 00} and {11 $\bar{2}$ 0} facets are 5.8 and 10.1 atoms/nm², as shown in figures 8(b) and (c), respectively. The coordinatively-unsaturated Fe cations on the surfaces, unlike the bulk Fe cations, can offer catalytically active

sites to generate $\cdot OH$ via the reaction between α -Fe₂O₃ and H₂O₂ [35], which can be described by the following equations.



In the photocatalytic reactions, the electrons are trapped by Fe³⁺ on the surfaces of NBs leading to the formation of Fe²⁺ cations (equation (8)). Then powerful oxidant hydroxyl radicals ($\cdot OH$) are produced through the reactions between Fe²⁺ cations and H₂O₂ (equation (9)). The photoinduced holes can be easily trapped by electron donors such as OH⁻ or organic dyes (equation (10)). According to the above equations, more exposed Fe cations can generate more $\cdot OH$ which could effectively oxidize the dye of RhB [34]. Therefore, more exposed Fe cations on the {1 $\bar{1}$ 00} and {11 $\bar{2}$ 0} surfaces of the single-layered reduced α -Fe₂O₃ NBs are considered as a key point in the improved photocatalytic performance.

To further study the enhanced photocatalytic activity of reduced NBs, we investigate the transient photocurrent responses from different Fe₂O₃ nanostructures using several on-off cycles of intermittent visible light irradiation. Figure 9 shows the photocurrent responses of reduced NBs, non-reduced NBs and α -Fe₂O₃ powder. It can be seen that the photocurrent density of the reduced NBs is about 1.3 times higher than that of non-reduced NBs and 2.36 times higher than that of α -Fe₂O₃ powder. The larger photocurrent for reduced NBs means a higher photoelectron transfer efficiency owing to enhanced visible light absorption and lower recombination of photogenerated electrons and holes.

Third, dislocations are believed to benefit the charge separation efficiency of photogenerated holes and electrons [36, 37]. In our study, perfect dislocations, observed in the single-layered reduced NBs, can be regarded as surface defects. According to the results from photocurrent responses, dislocations can act as active sites for absorption of electron

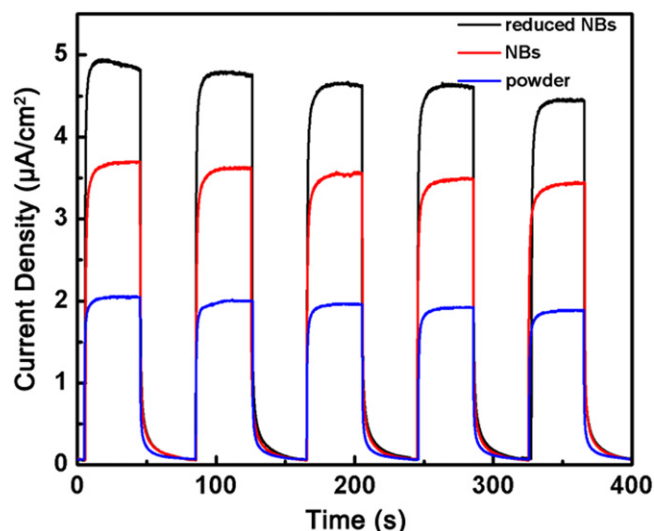


Figure 9. Current density responses of different Fe_2O_3 nanostructures under intermittent irradiation at a bias potential of 0.2 V versus Ag/AgCl ($\lambda > 420$ nm).

acceptors or donors. Therefore, charge separation efficiency can be improved by the dislocations in the reduced NBs, and thus the photocatalytic activities can be enhanced.

Based on the above analyses, the enhanced photocatalytic performance could be rationalized by the defects with different dimensions such as point defects (oxygen vacancies), linear defects (dislocations) and bulk defects (pores) in the reduced single-layered $\alpha\text{-Fe}_2\text{O}_3$ NBs. In contrast to previous studies [29, 38, 39] focusing on effects of different facets on the photocatalytic activities of $\alpha\text{-Fe}_2\text{O}_3$ nanostructures, our findings demonstrate that microstructural defects are also crucial for the design of high-performance nanocatalysts.

Conclusions

In summary, bicrystalline $\alpha\text{-Fe}_2\text{O}_3$ NBs with CSL boundaries were produced on a large scale through thermal oxidation of Fe foils. The thermal reduction of these bicrystalline $\alpha\text{-Fe}_2\text{O}_3$ NBs in vacuum converts a double-layered structure into a single-layered structure. Due to the formation of oxygen vacancies, perfect dislocations and dense pores in the reduced single-layered $\alpha\text{-Fe}_2\text{O}_3$ NBs, visible-light-induced RhB degradation in the presence of H_2O_2 is significantly enhanced. These reduced NBs can be used to degrade organic pollutants in industrial waste water. Considering the unique structures of reduced NBs, we believe that our work will open up new ways to systematically fabricate other reduced nanostructures such as nanowires and nanoparticles. In addition, the reduction of other metal-oxide (e.g. ZnO and SnO_2) nanostructures could also produce efficient photocatalysts. Furthermore, this study has broad implications in hematite-based water-splitting and solar cells, among others.

Acknowledgments

The authors are grateful to the National Key Basic Research Development Program of China (Grant no.: 2012CB722705), the Natural Science Foundation for Outstanding Young Scientists in Shandong Province, China (Grant no.: JQ201002), and High-end Foreign Experts Recruitment Program (Grant nos.: GDW20143500163, GDW20133400112) for financial support. YQW would also like to acknowledge financial support from the Top-notch Innovative Talent Program of Qingdao City (Grant no.: 13-CX-8), and the Taishan Scholar Program of Shandong Province, China. The work at SUNY Binghamton was supported by the National Science Foundation under NSF CAREER Award Grant CMMI-1056611. FR acknowledges funding and salary support from NSERC through a Discovery Grant and an EWR Steacie Memorial Fellowship.

References

- [1] Rosei F 2004 Nanostructured surfaces: challenges and frontiers in nanotechnology *J. Phys. Condens. Matter* **16** S1373
- [2] Yan C L, Nikolova L, Dadvand A, Harnagea C, Sarkissian A, Perepichka D F, Xue D F and Rosei F 2010 Multiple $\text{NaNbO}_3/\text{Nb}_2\text{O}_5$ heterostructure nanotubes: a new class of ferroelectric/semiconductor nanomaterials *Adv. Mater.* **22** 1741
- [3] Zhao Y, Feng Z X and Xu Z C J 2015 Yolk-shell Fe_2O_3 circle dot C composites anchored on MWNTs with enhanced lithium and sodium storage *Nanoscale* **7** 9520
- [4] Chen G Z, Rosei F and Ma D L 2012 Interfacial reaction-directed synthesis of Ce-Mn binary oxide nanotubes and their applications in CO oxidation and water treatment *Adv. Funct. Mater.* **22** 3914
- [5] Dembele K T *et al* 2015 Graphene below the percolation threshold in TiO_2 for dye-sensitized solar cells *J. Mater. Chem. A* **3** 2580
- [6] Nechache R, Harnagea C, Li S, Cardenas L, Huang W, Chakrabarty J and Rosei F 2015 Bandgap tuning of multiferroic oxide solar cells *Nat. Photonics* **9** 61
- [7] Zhou X M, Xu Q L, Lei W Y, Zhang T T, Qi X Y, Liu G, Deng K and Yu J G 2014 Origin of tunable photocatalytic selectivity of well-defined $\alpha\text{-Fe}_2\text{O}_3$ nanocrystals *Small* **10** 674
- [8] Yang S H, Song X F, Zhang P, Sun J and Gao L 2014 Self-assembled $\alpha\text{-Fe}_2\text{O}_3$ mesocrystals/graphene nanohybrid for enhanced electrochemical capacitors *Small* **10** 2270
- [9] Brezesinski K, Haetge J, Wang J, Mascotto S, Reitz C, Rein A, Tolbert S H, Perlich J, Dunn B and Brezesinski T 2011 Ordered mesoporous $\alpha\text{-Fe}_2\text{O}_3$ (hematite) thin-film electrodes for application in high rate rechargeable lithium batteries *Small* **7** 407
- [10] Mor G K, Prakasam H E, Varghese O K, Shankar K and Grimes C A 2007 Vertically oriented Ti-Fe-O nanotube array films: toward a useful material architecture for solar spectrum water photoelectrolysis *Nano Lett.* **7** 2356
- [11] Barroso M, Cowan A J, Pendlebury S R, Grätzel M, Klug D R and Durrant J R 2011 The role of cobalt phosphate in enhancing the photocatalytic activity of $\alpha\text{-Fe}_2\text{O}_3$ toward water oxidation *J. Am. Chem. Soc.* **133** 14868
- [12] Apte S K, Naik S D, Sonawane R S and Kale B B 2007 Synthesis of nanosize-necked structure α - and γ -

- Fe₂O₃ and its photocatalytic activity *J. Am. Ceram. Soc.* **90** 412
- [13] Li L L, Chu Y, Liu Y and Dong L H 2007 Template-free synthesis and photocatalytic properties of novel, Fe₂O₃ hollow spheres *J. Phys. Chem. C* **111** 2123
- [14] Peng L L, Xie T F, Lu Y C, Fan H M and Wang D J 2010 Synthesis, photoelectric properties and photocatalytic activity of the Fe₂O₃/TiO₂ heterogeneous photocatalysts *Phys. Chem. Chem. Phys.* **12** 8033
- [15] Li L and Koshizaki N 2010 Vertically aligned and ordered hematite hierarchical columnar arrays for applications in field-emission, superhydrophilicity, and photocatalysis *J. Mater. Chem.* **20** 2972
- [16] Wang L, Wei H W, Fan Y J, Gu X and Zhan J H 2009 One-dimensional CdS/alpha-Fe₂O₃ and CdS/Fe₃O₄ heterostructures: epitaxial and nonepitaxial growth and photocatalytic activity *J. Phys. Chem. C* **113** 14119
- [17] Yuan L, Jiang Q K, Wang J B and Zhou G W 2012 The growth of hematite nanobelts and nanowires-tune the shape via oxygen gas pressure *J. Mater. Res.* **27** 1014
- [18] Yuan L, Wang Y Q, Cai R S, Jiang Q K, Wang J B, Li B Q, Sharma A and Zhou G W 2012 The origin of hematite nanowire growth during the thermal oxidation of iron *Mater. Sci. Eng. B* **177** 327
- [19] Yuan L, Cai R S, Jang J I, Zhu W H, Wang C, Wang Y Q and Zhou G W 2013 Morphological transformation of hematite nanostructures during oxidation of iron *Nanoscale* **5** 7581
- [20] Wang Y Q, Wang C, Yuan L, Cai R S, Liu X H, Li C Y and Zhou G W 2014 Coincidence-site-lattice twist boundaries in bicrystalline alpha-Fe₂O₃ nanoblades *J. Phys. Chem. C* **118** 5796
- [21] Zheng Y H, Chen C Q, Zhan Y Y, Lin X Y, Zheng Q, Wei K M, Zhu J F and Zhu Y J 2007 Luminescence and photocatalytic activity of ZnO nanocrystals: correlation between structure and property *Inorg. Chem.* **46** 6675
- [22] Lukowski M A and Jin S 2011 Improved synthesis and electrical properties of Si-doped alpha-Fe₂O₃ nanowires *J. Phys. Chem. C* **115** 12388
- [23] Lanier C H, Chiamonti A N, Marks L D and Poeppelmeier K R 2009 The Fe₃O₄ origin of the 'biphase' reconstruction on alpha-Fe₂O₃ (0001) *Surf. Sci.* **603** 2574
- [24] Colliex C, Manoubi T and Ortiz C 1991 Electron-energy-loss-spectroscopy near-edge fine structures in the iron-oxygen system *Phys. Rev. B* **44** 11402
- [25] Chueh Y L, Lai M W, Liang J Q, Chou L J and Wang Z L 2006 Systematic study of the growth of aligned arrays of alpha-Fe₂O₃ and Fe₃O₄ nanowires by a vapor-solid process *Adv. Funct. Mater.* **16** 2243
- [26] Pearson D H, Fultz B and Ahn C C 1988 Measurements of 3d state occupancy in transition metals using electron energy loss spectrometry *Appl. Phys. Lett.* **53** 1405
- [27] Hirsch P, Howie A, Nicholson R B, Pashley D W, Whelan M J and Robert E 1977 *Electron Microscopy of Thin Crystals* (Huntington NY: Kreiger) pp 384
- [28] Kim D H, Lee H J, Kim G, Koo Y S, Jung J H, Shin H J, Kim J Y and Kang J S 2009 Interface electronic structures of BaTiO₃@X nanoparticles (X = gamma-Fe₂O₃, Fe₃O₄, alpha-Fe₂O₃, and Fe) investigated by XAS and XMCD *Phys. Rev. B* **79** 033402
- [29] Zhou X M, Lan J Y, Liu G, Deng K, Yang Y L, Nie G J, Yu J G and Zhi L J 2012 Facet-mediated photodegradation of organic dye over hematite architectures by visible light *Angew. Chem. Int. Ed.* **124** 182
- [30] Ivanova I, Schneider J, Gutzmann H, Kliemann J O, Gärtner F, Klassen T, Bahnemann D and Mendive C B 2013 Photocatalytic degradation of oxalic and dichloroacetic acid on TiO₂ coated metal substrates *Catal. Today* **209** 84
- [31] Fateh R, Dillert R and Bahnemann D 2013 Preparation and characterization of transparent hydrophilic photocatalytic TiO₂/SiO₂ thin films on polycarbonate *Langmuir* **29** 3730
- [32] Guo H L, Zhu Q, Wu X L, Jiang Y F, Xie X and Xu A W 2015 Oxygen deficient ZnO_{1-x} nanosheets with high visible light photocatalytic activity *Nanoscale* **7** 7216
- [33] Lv Y H, Liu Y F, Zhu Y Y and Zhu Y F 2014 Surface oxygen vacancy induced photocatalytic performance enhancement of a BiPO₄ nanorod *J. Mater. Chem. A* **2** 1174
- [34] Lin X P, Huang T, Huang F Q, Wang W D and Shi J L 2006 Photocatalytic activity of a Bi-based oxychloride Bi₃O₄Cl *J. Phys. Chem. B* **110** 24629
- [35] Brillas E, Sirés I and Oturan M A 2009 Electro-fenton process and related electrochemical technologies based on Fenton's reaction chemistry *Chem. Rev.* **109** 6570
- [36] Li Y X, Chen G, Wang Q, Wang X, Zhou A K and Shen Z Y 2010 Hierarchical ZnS-In₂S₃-CuS nanospheres with nanoporous structure: facile synthesis, growth mechanism, and excellent photocatalytic activity *Adv. Funct. Mater.* **20** 3390
- [37] Li C Y, Wang J B and Wang Y Q 2012 Microstructure and photocatalytic activity of titanium dioxide nanoparticles *Chin. Phys. B* **21** 098102
- [38] Zhao Y B, Pan F, Li H, Niu T C, Xu G Q and Chen W 2013 Facile synthesis of uniform alpha-Fe₂O₃ crystals and their facet-dependent catalytic performance in the photo-Fenton reaction *J. Mater. Chem. A* **1** 7242
- [39] Wang X, Wang J Q, Cui Z T, Wang S G and Cao M H 2014 Facet effect of alpha-Fe₂O₃ crystals on photocatalytic performance in the photo-Fenton reaction *RSC Adv.* **4** 34387